Theoretical investigation of the phonon-limited carrier mobility in (001) Si films

Jing Li, Evelyne Lampin, Christophe Delerue, Yann-Michel Niquet

Journal of Applied Physics

Theoretical investigation of the phonon-limited carrier mobility in (001) Si films

Cite as: J. Appl. Phys. **120**, 174301 (2016); https://doi.org/10.1063/1.4966616
Submitted: 19 July 2016 • Accepted: 18 October 2016 • Published Online: 03 November 2016

Jing Li, Evelyne Lampin, Christophe Delerue, et al.

AIP Publishing

JOURNAL OF APPLIED PHYSICS **120**, 174301 (2016)

Theoretical investigation of the phonon-limited carrier mobility in (001) Si films

Jing Li,[1,a)] Evelyne Lampin,[2] Christophe Delerue,[2,b)] and Yann-Michel Niquet[1,c)]
[1]*Univ. Grenoble Alpes, INAC-, L_Sim, Grenoble, France and CEA, INAC-MEM, L_Sim, Grenoble, France*
[2]*IEMN, UMR CNRS 8520, Villeneuve d'Ascq, France*

(Received 19 July 2016; accepted 18 October 2016; published online 3 November 2016)

We calculate the phonon-limited carrier mobility in (001) Si films with a fully atomistic framework based on a tight-binding (TB) model for the electronic structure, a valence-force-field model for the phonons, and the Boltzmann transport equation. This framework reproduces the electron and phonon bands over the whole first Brillouin zone and accounts for all possible carrier-phonon scattering processes. It can also handle one-dimensional (wires) and three-dimensional (bulk) structures and therefore provides a consistent description of the effects of dimensionality on the phonon-limited mobilities. We first discuss the dependence of the electron and hole mobilities on the film thickness and carrier density. The mobility tends to decrease with decreasing film thickness and increasing carrier density, as the structural and electric confinement enhances the electron-phonon interactions. We then compare hydrogen-passivated and oxidized films in order to understand the impact of surface passivation on the mobility and discuss the transition from nanowires to films and bulk. Finally, we compare the semi-classical TB mobilities with quantum Non-Equilibrium Green's Function calculations based on $k \cdot p$ band structures and on deformation potentials for the electron-phonon interactions (KP-NEGF). The TB mobilities show a stronger dependence on carrier density than the KP-NEGF mobilities, yet weaker than the experimental data on Fully Depleted-Silicon-on-Insulator devices. We discuss the implications of these results on the nature of the apparent increase of the electron-phonon deformation potentials in silicon thin films. *Published by AIP Publishing.*
[http://dx.doi.org/10.1063/1.4966616]

I. INTRODUCTION

For more than 50 years, silicon Field-Effect Transistors (FETs) have been the cornerstone of the digital revolution. The continuous downscaling of the gate length has enabled considerable improvement of the integrated circuit performances.[1] However, extreme scaling below 20 nm calls for innovative device architectures[2] in order to reduce short channel effects. In this context, fully depleted silicon on insulator (FDSOI) transistors based on silicon thin films are an attractive alternative to bulk Metal-Oxide-Semiconductor FETs (MOSFETs).[3–12] In FDSOI devices, the thickness of the channel is well below 10 nm, so that structural confinement effects can be significant. Quantum modeling has, therefore, become an important tool for their design and understanding,[6,13–26] as was already the case for bulk MOSFETs in the strong inversion regime.[27–36] But quantum simulations are still based on severe approximations and free parameters that must be assessed using detailed comparisons with experiments[23] or more advanced modeling schemes.

In this paper, we present semi-classical Kubo-Greenwood (KG) calculations of the low-field phonon-limited electron and hole mobilities in silicon thin films. In contrast to previous studies, and in line with our recent works on bulk Si[37] and Si nanowires,[38–40] we use a fully atomistic description of the electron and phonon wave-functions and account for all possible carrier-phonon interactions. We achieve that way a consistent description of electron-phonon interactions in bulk, film, and wire structures. We investigate, in particular, the effects of the oxidation on the mobility and the transition between two-dimensional (2D) films and one-dimensional (1D) nanowires. We compare these semi-classical results with quantum Non-Equilibrium Green's Functions (NEGF) calculations based on $\mathbf{k} \cdot \mathbf{p}$ models for the band structure and on deformation potentials for the electron-phonon interactions. We discuss open issues about the mechanisms that limit the mobility in FDSOI devices, in particular, the strong enhancement of the interaction with acoustic phonons that must usually be introduced in deformation potential theories in order to reproduce the experimental data.

The paper is organized as follows. In Sec. II, we describe the model FDSOI device considered in this work (Sec. II A), and then the methodology for the semi-classical atomistic calculations (Sec. II B) and for the quantum NEGF calculations (Sec. II C). The mobility in Si films passivated by hydrogen atoms is discussed in Sec. III, and the mobility in oxidized Si films in Sec. IV. The transition from 2D (Si films) to 1D (Si nanowires) is then investigated in Sec. V. Finally, in Sec. VI, we compare KG and NEGF calculations and discuss the problem of the enhancement of the acoustic deformation potentials.

[a)]Electronic mail: jing.li.phy@gmail.com
[b)]Electronic mail: christophe.delerue@iemn.univ-lille1.fr
[c)]Electronic mail: yniquet@cea.fr

II. METHODOLOGY

A. Model for the FDSOI device

A schematic view of the modeled FDSOI devices is shown in Fig. 1.[23] A (001)-oriented Si film with thickness t_{Si} is embedded between front- and back-gate stacks. The front-gate stack is made of a 2.4 nm thick layer of SiO_2 and a 1.8 nm thick layer of HfO_2. The buried back-gate oxide is 25 nm thick. We assume that the back-gate is grounded.

B. Atomistic calculations of the mobility

The methodology for the atomistic modeling of the phonon-limited mobility in Si films is fundamentally the same as in our previous works on Si nanowires.[38–40] However, calculations for 2D systems are computationally more challenging because they require 2D integrations in k space while the number of electron and phonon bands that must be considered remains very large. Details are given below and in the Appendix A.

We use the $sp^3d^5s^*$ tight-binding (TB) model of Ref. 41 for the electronic structure of the Si films. This model reproduces the main band gaps, effective masses, and deformation potentials of bulk silicon (see also Appendix B). Spin-orbit coupling is included for the holes. Except otherwise stated, we assume that the surfaces of the Si films are passivated by pseudo-hydrogen atoms. The pseudo-hydrogen atoms are characterized by a single s orbital with energy $E_H = 0.175$ eV and nearest-neighbor Si-H hopping terms $V_{ss\sigma} = -4.129$ eV and $V_{sp\sigma} = 3.723$ eV (notations of Ref. 42).[43]

The band structure, charge density, and electrostatic potential in the device are calculated self-consistently in a Schrödinger-Poisson approach. The Poisson equation is solved on a regular mesh with a step of 1 Å. The dielectric constants of HfO_2, SiO_2, silicon, and buried oxide are set to 20.0, 5.2, 11.7, and 3.9, respectively. The charge in each mesh element is obtained from the TB wave functions.

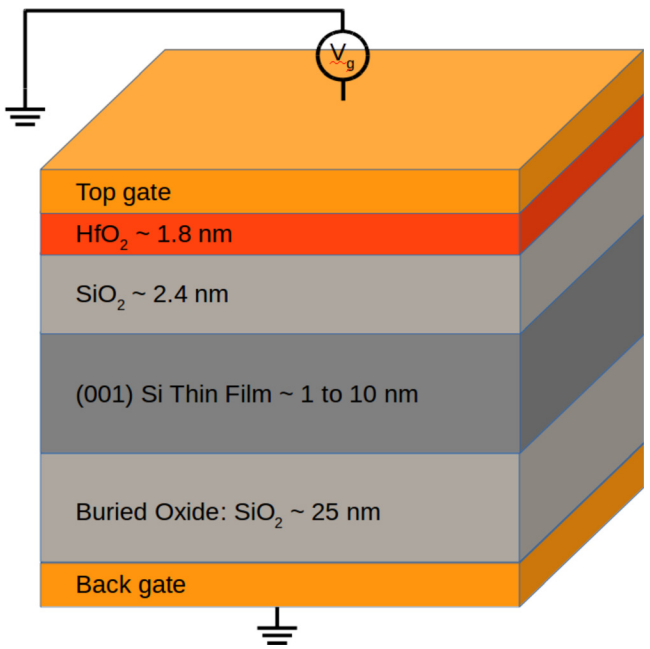

FIG. 1. Schematic view of a FDSOI device. The back gate is grounded, and the bias is applied to the top gate.

The phonon dispersion and phonon wave functions are computed with the valence-force-field (VFF) model of Vanderbilt *et al.*[44,45]

We scan the electron and phonon band structures for all possible carrier-phonon scattering processes where an electron (hole) moves from an initial to a final state and concomitantly a phonon is either absorbed or emitted (energy and momentum must be conserved). Initial and final electronic states are sampled within a range of $\pm 10 k_B T$ around the Fermi level, where k_B is the Boltzmann constant and T is the temperature. Umklapp scattering processes are taken into account. Details can be found in Appendix A.

The electron-phonon interactions are proportional to the derivatives of the TB Hamiltonian with respect to the atomic positions. The scattering rates are computed from these derivatives, the carrier and the phonon wave functions with the Fermi golden rule. The mobility is then obtained from an exact solution of Boltzmann's transport equation.[38] In bulk Si, the calculated electron mobility ($\mu = 1407\ cm^2/V\ s$) is in excellent agreement with the experiment ($\mu_{exp} \simeq 1400\ cm^2/V\ s$), but the hole mobility ($\mu = 678\ cm^2/V\ s$) is overestimated ($\mu_{exp} \simeq 500\ cm^2/V\ s$).[39]

C. NEGF calculations

We have performed NEGF simulations based on a continuous –instead of atomistic –description, for comparison. The methodology[46] is described in Refs. 24 and 23. The conduction band structure of the Si films is calculated using a two-band $\mathbf{k} \cdot \mathbf{p}$ model (2KP).[47] At variance with the effective mass approximation (EMA), the 2KP model accounts for non-parabolic corrections. We have checked that the 2KP conduction band structures are in good agreement with TB. The EMA mobilities (not shown) are systematically larger than the 2KP mobilities, which highlights the importance of non-parabolic corrections.[29,30,48] The valence band structure is calculated with a six-band $\mathbf{k} \cdot \mathbf{p}$ model (6KP).[24]

For electrons, the intra-valley acoustic phonon scattering is described by an isotropic deformation potential Ξ_{ac}^e (Appendix B). We also consider inter-valley optical phonon scattering by the 3 f-type and 3 g-type processes of Ref. 49. For holes, we use a diagonal hole-phonon interaction with one single acoustic deformation potential Ξ_{ac}^h and one single optical deformation potential $DK_{op} = 15$ eV/Å (optical phonon energy $E_{op} = 63$ meV).[33,50] In all cases, the electron-phonon interactions are limited to local self-energies.[23,50,51]

For reasons that will be discussed in Sect. VI A, we consider two sets of acoustic phonon deformation potentials: $\Xi_{ac}^e = 9$ eV and $\Xi_{ac}^h = 10.2$ eV, which are the usual values for bulk Si, and $\Xi_{ac}^e = 14.6$ eV and $\Xi_{ac}^h = 15.5$ eV, which yield NEGF carrier mobilities in better agreement with experiments on FDSOI devices.[24]

III. RESULTS FOR Si FILMS PASSIVATED BY HYDROGEN ATOMS

In the following, we discuss the electron and hole mobilities in Si films with thickness t_{Si} ranging from 1 to 10 nm, and

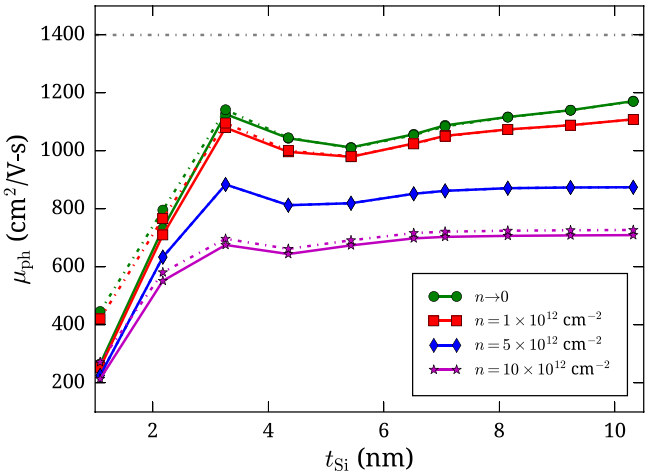

FIG. 2. Phonon-limited electron mobility as a function of the film thickness. Solid lines represent the mobility in the $[1\bar{1}0]$ direction, dashed lines the mobility in the [110] direction. The horizontal line at 1407 cm^2/V s indicates the bulk Si mobility.

for four carrier densities, $n \to 0$,[52] $n = 10^{12}$, $n = 5 \times 10^{12}$, and $n = 10^{13}$ cm^{-2}. The mobilities are calculated for an electric field applied along the [110] and $[1\bar{1}0]$ directions, i.e., along the principal in-plane crystallographic axes of the Si films.

A. Electron mobility

The phonon-limited electron mobility is plotted as a function of t_{Si} in Fig. 2. There is a small difference between the mobility μ_{110} along [110] and $\mu_{1\bar{1}0}$ along $[1\bar{1}0]$, especially at high carrier density and in thin films. In bulk Si, the mobility is the same in the two directions, which are crystallographically equivalent. The symmetry is broken in ideal (001) films, since there are two different kinds of (001) surfaces in a diamond lattice: the bonds connecting the Si atoms to the hydrogens (or embedding material) are, indeed, all aligned either along [110] or along $[1\bar{1}0]$. Under high inversion bias or strong confinement, the carrier wave functions are pushed towards the top surface, as shown in Fig. 3. In these

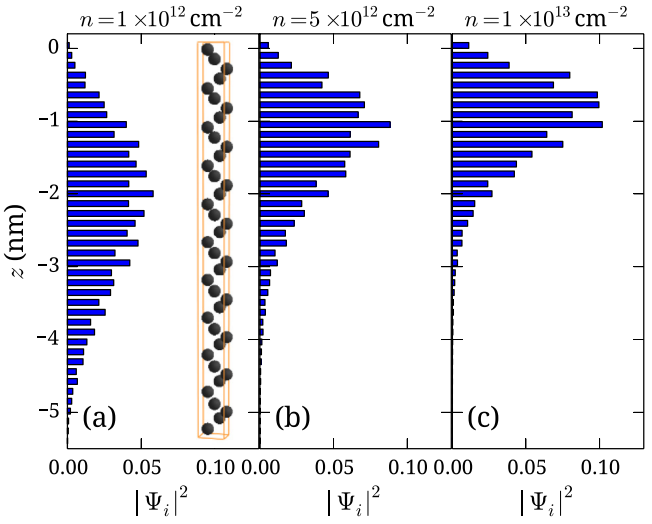

FIG. 3. The unit cell of a Si film ($t_{Si} = 5$ nm, inset of (a)) and the squared electron wave function of the conduction band minimum at different bias corresponding to (a) $n = 10^{12}$, (b) $n = 5 \times 10^{12}$, and (c) $n = 10^{13}$ cm^{-2}.

conditions, the transport properties become sensitive to the symmetry of the surface (or interface). Experimentally, this small anisotropy shall, however, be washed out by surface roughness.

Figure 2 shows that the electron mobility exhibits a similar behavior at all densities. The mobility is very low in the thinnest films, then rises and reaches a maximum near $t_{Si} = 3$ nm, and finally shows a dip near $t_{Si} = 5$–6 nm. The mobility at low density slowly increases with $t_{Si} > 6$ nm and reaches 1225 cm^2/V s for $t_{Si} = 14$ nm (not shown[53]), still far from the bulk value (1400 cm^2/V s). However, the mobility saturates above a certain t_{Si} at high carrier densities. This saturation results from the localization of the electron gas near the top interface under the effect of the electric field (Fig. 3). As a consequence, the effective film thickness probed by the electrons becomes practically independent of the nominal film thickness, and the mobility is degraded like in thinner films. Therefore, we basically recover the situation of bulk Si MOSFETs in the strong inversion regime.[7,28–30,54,55]

The poor mobility in ultimate films ($t_{Si} < 3$ nm) is known to result from the strong confinement of the electrons, which increases the overlap between the squared wave functions of the confined initial and final states, hence the electron-phonon interactions.[7,13,56] A very similar behavior has been predicted in thin Si nanowires.[18,38–40,48,57,58] The mobility tends to decrease with increasing carrier density for two reasons. First, the interactions between the electrons and acoustic phonons get enhanced when the electron are more confined, as discussed above. Second, the density of possible final states for scattering (hence the scattering rates) increases with increasing carrier energy.

The peak near $t_{Si} \approx 3$ nm and the small dip above have been observed in FDSOI devices.[7] This behavior results from the effects of quantum confinement on the band structure of (001) Si films,[7,25] as illustrated in Fig. 4. The six equivalent conduction band valleys of bulk silicon indeed split into two groups. The two Δ_z valleys project onto Γ ($\mathbf{k} = 0$) in the 2D Brillouin zone of the film, while the Δ_x and Δ_y valleys fold near the corners of the Brillouin zone. Moreover, the $\Delta_{x,y}$ valleys, which are confined along the light transverse mass axis, lie at higher energy than the Δ_z valleys, which are confined along the heavy longitudinal mass axis (but show a lighter transport mass). The difference ΔE between the energies of the Δ_z and $\Delta_{x,y}$ conduction band minima strongly depends on t_{Si} in thin films (Fig. 4(a)). When $t_{Si} \lesssim 3$ nm, ΔE is large enough so that the electrons mostly occupy the light Δ_z valleys at Γ. In addition, ΔE is larger than the optical phonon energy (about 63 meV), which inhibits inter-valley scattering. When t_{Si} is increased, ΔE drops below 63 meV, so that inter-valley scattering is enhanced. Also, the electrons progressively occupy the four valleys at $\mathbf{k} \neq 0$ characterized by a heavier transport mass. Meanwhile, the acoustic phonon scattering rates decrease as $1/t_{Si}$.[7,13,29] The combination of these opposite effects explains the mobility peak near $t_{Si} \simeq 3$ nm, the dip in the mobility near 4–5 nm, and the rise or the saturation above.

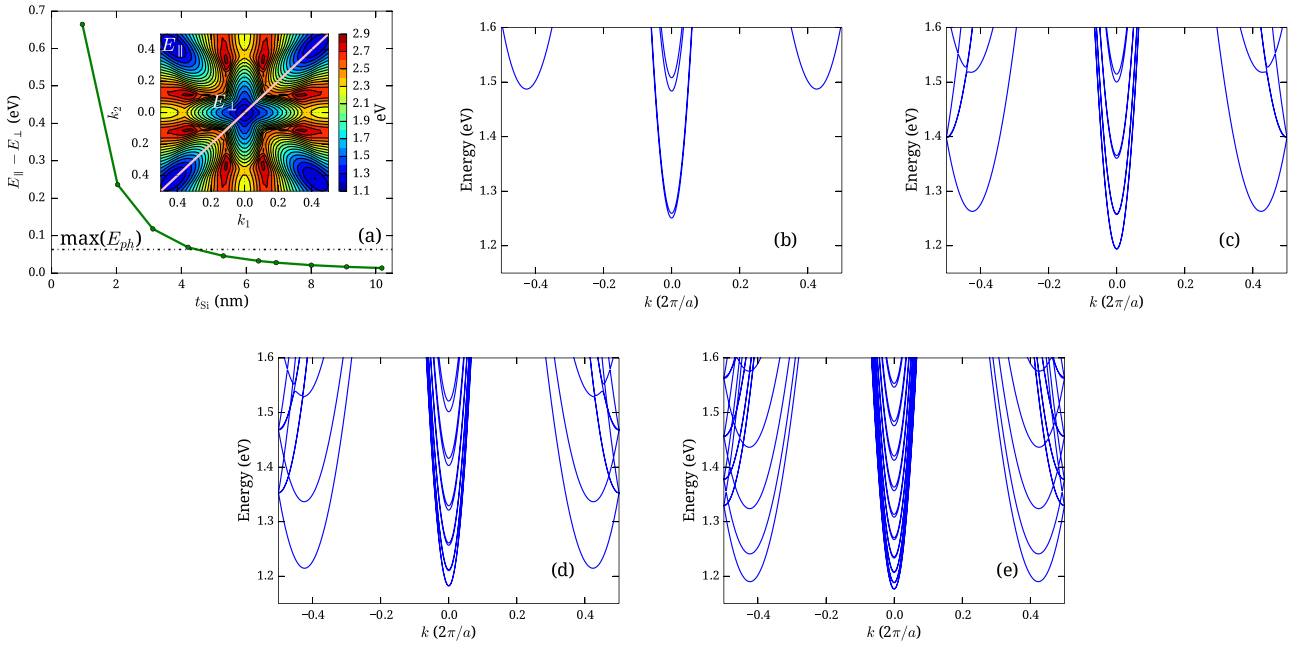

FIG. 4. (a) Energy difference $\Delta E = E_{\parallel} - E_{\perp}$ between the fourfold degenerate (Δ_x, Δ_y) and the twofold degenerate (Δ_z) valleys. The horizontal line is the highest phonon energy. Inset: Contour plot of the lowest conduction band energy in the first Brillouin zone (k_1 is along $[1\bar{1}0]$, k_2 along $[110]$); $E_{\parallel}$ indicates one of the fourfold degenerate $\Delta_{x,y}$ valley; $E_{\perp}$ the twofold degenerate Δ_z valley at Γ. The band structure of the film is plotted along $[100]$ (pink line) for $t_{Si} = 2$ nm (b), 4 nm (c), 6 nm (d), and 10 nm (e).

B. Hole mobility

The size-dependent hole mobility calculated in TB is plotted in Fig. 5(a). Again, it presents a sizable anisotropy along the $[110]$ and $[1\bar{1}0]$ directions. The anisotropy is small at low carrier density but, in contrast to electrons, becomes huge at high carrier density. This behavior also results from the low symmetry of the ideal (001) surfaces, which translates into a strong anisotropy of the topmost valence bands (Fig. 6(a)). The highest valence band (which has a dominant "heavy-hole" $|3/2, \pm 3/2\rangle$ character) indeed shows a much lighter mass along the $[1\bar{1}0]$ than along the $[110]$ direction. The situation is reversed for the second band. This picture is supported by *ab initio* calculations. The anisotropy of the topmost valence bands is negligible at small carrier density but increases with increasing carrier density as the holes are pushed towards the top surface of the film (Fig. 6(c)). Note that the mobility along $[100]$ and $[010]$ is simply $\bar{\mu} = \mu_{100} = \mu_{010} = (\mu_{110} + \mu_{1\bar{1}0})/2$.

As expected from the above mechanism, the anisotropy of the topmost valence bands and of the hole mobility are strongly dependent on the passivation of the Si film. It is, in particular, possible to adjust the TB parameters of the pseudo-hydrogen atoms so that the topmost valence bands are almost isotropic ($E_H = 2.925$ eV, $V_{ss\sigma} = -3.0$ eV, and $V_{sp\sigma} = 5.2$ eV, see Fig. 6(b)). Interestingly, the mobility calculated in that case (hollow markers in Fig. 5(b)) is very close to $\bar{\mu}$ –in other words, $\bar{\mu}$ is little sensitive to the passivation of the film, at variance with the difference $\mu_{110} - \mu_{1\bar{1}0}$. We will investigate the effects of surface passivation in more detail in Section IV.

Again, in practical devices the anisotropy of the mobility shall be washed out by surface roughness. In the following, we therefore take $\bar{\mu}$ as an estimate of the mobility in FDSOI devices.

For $t_{Si} \lesssim 2$ nm, $\bar{\mu}$ is small and is almost the same for all densities. $\bar{\mu}$ increases continuously with t_{Si} in the low density regime (Fig. 5) and should reach the bulk value for $t_{Si} \gg 10$ nm. However, for $n \geq 5 \times 10^{12}$ cm^{-2}, the mobility quickly saturates at relatively small values compared to the bulk. Like electrons, the holes are strongly confined near the top surface by the electric field, so that their mobility becomes independent of t_{Si} and is low because of a stronger coupling to acoustic phonons.

IV. RESULTS ON Si FILMS WITH OXIDIZED SURFACE

In this section, we investigate the effect of the surface passivation on the electron mobility by considering two models for oxidized surfaces (Sec. IV A). The atomic structure of these models is not relaxed using the VFF model of Vanderbilt *et al.*,[45] but using the Tersoff interatomic potential[59] because a parameterization is available for systems with Si-O bonds.[60] Tersoff parameters for Si-H bonds are taken from Ref. 61. The same potential is used to calculate the phonon band structure and wave functions needed as input for the scattering rates. The structural relaxation and the phonons are computed with GULP.[62] In Sec. IV B, we show that the nature of the interatomic potential used to describe the phonons has a substantial influence on the electron mobility in H-passivated films. The comparison between mobilities calculated for H-passivated and oxidized surfaces is discussed in Sec. IV C.

A. Models of oxidized surfaces

The first model (Model 1) of an oxidized surface is depicted in Fig. 7(a). We start from a (001) film of Si. On the top surface, we remove one $[100]$ line of Si atoms out of two, and the dangling bonds on the Si atoms of the sub-surface

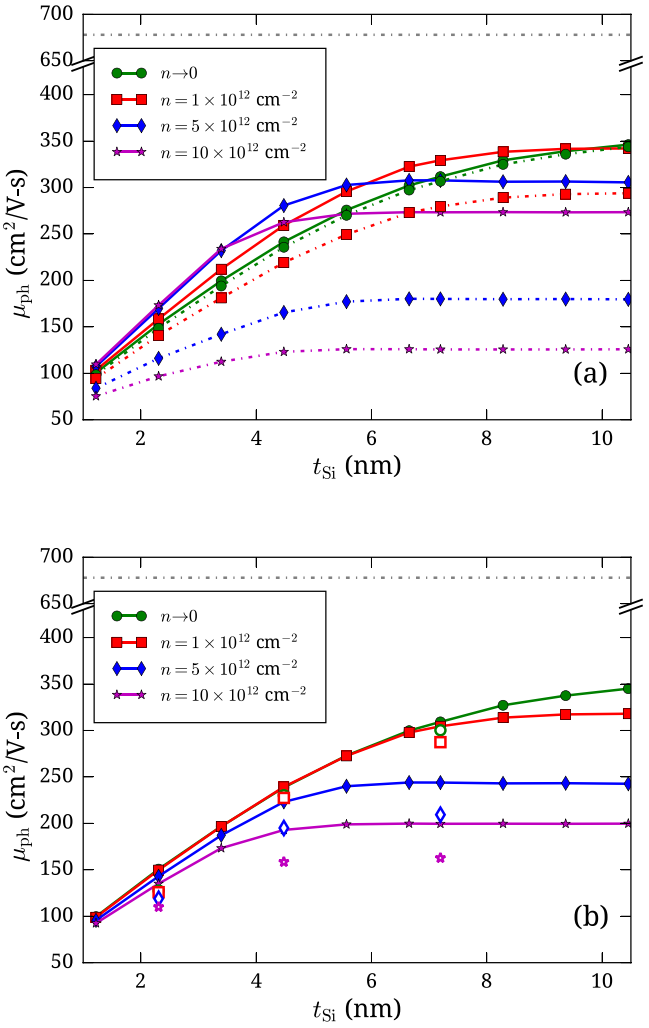

FIG. 5. (a) Phonon-limited hole mobility as a function of film thickness. Solid lines represent the mobility $\mu_{1\bar{1}0}$ along $[1\bar{1}0]$, dashed lines the mobility μ_{110} along $[110]$; (b) Average mobility $\bar{\mu}$ defined as $\bar{\mu}$ as $\bar{\mu} = (\mu_{110} + \mu_{1\bar{1}0})/2$. The hollow markers represent the mobility calculated with pseudo-hydrogen parameters such that the topmost valence bands are almost isotropic. The horizontal line at 678 cm^2/V s indicates the calculated bulk Si mobility.

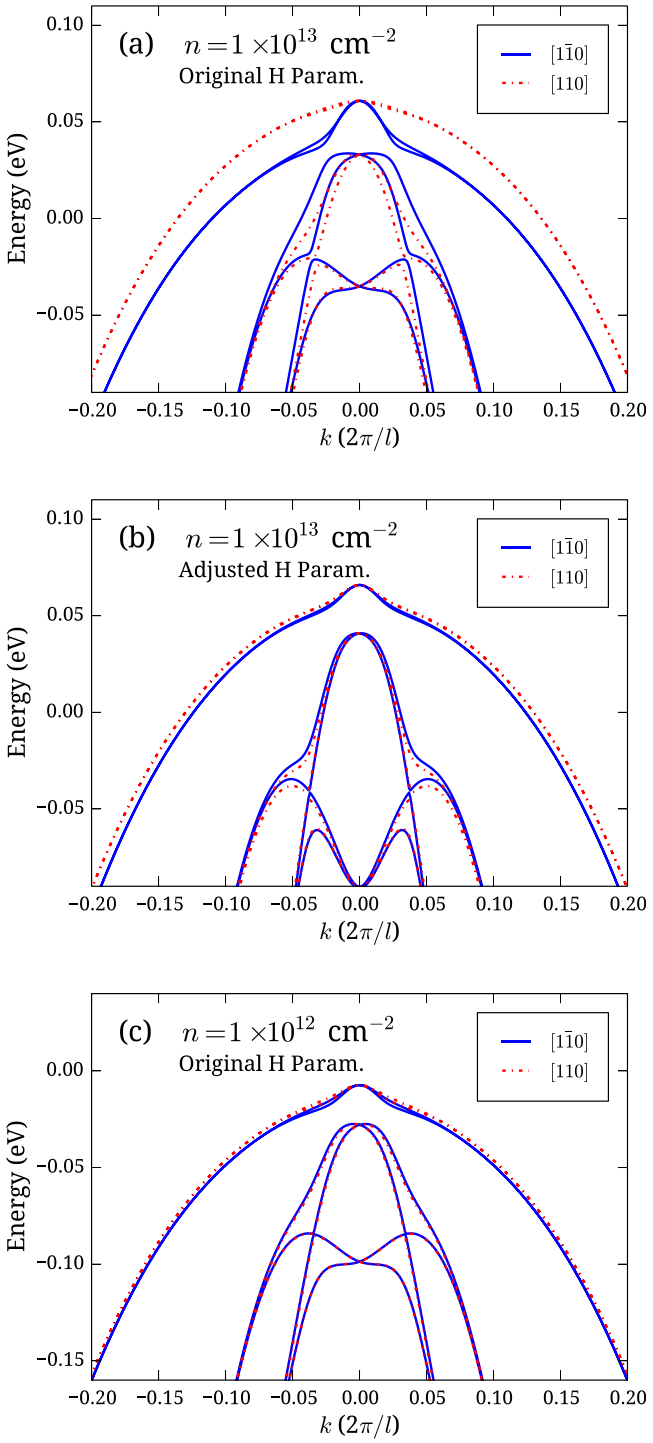

FIG. 6. Valence band structure calculated for $t_{Si} = 2$ nm (a) with the TB parameters of Ref. 43 for pseudo-hydrogen atoms, (b) with the TB parameters for pseudo-hydrogen atoms adjusted so that the highest valence band is almost isotropic at $n = 1 \times 10^{13}$ cm^{-2}. (c) Same as (a) but at low carrier density ($n = 1 \times 10^{12}$ cm^{-2}). Blue solid lines: $\mathbf{k} \parallel [1\bar{1}0]$. Red dashed lines: $\mathbf{k} \parallel [110]$.

plane are saturated by hydrogen atoms. The dangling bonds of the surface atoms are saturated by O-Si-H_2 radicals and, in each pair of radicals connected to the same Si atom of the surface, bonds are created to form a Si dimer. The opposite surface of the film is defined symmetrically.

The second model (Model 2, Fig. 7(b)) is based on the well-known (2×1) reconstruction of the (001) surface by dimerization. In this reconstruction, pairs of Si atoms, originally second-nearest neighbors, move to nearest-neighbor positions to form a covalent bond, and rows of dimers are formed along the $[1\bar{1}0]$ direction. The partial oxidation is done here by introducing an oxygen atom at the center of each dimer, relaxing the strain in the back bonds. This leads to the formation of oxygen bridges between the Si atoms, which almost come back to their original second-nearest neighbor position, a configuration that has been widely studied in the literature (e.g., in Refs. 63 and 64). The remaining dangling bonds (one per Si atom of the surface) are passivated by hydrogen atoms. Once again, the opposite surface of the film is defined symmetrically.

These two models have been chosen not only for their simplicity but also in order to avoid strains in the film that could be induced by the oxidation of the surface. There is no strain here because the oxide layer is discontinuous in the plane of the surface. We have also tried to consider more elaborate models for the oxide that are continuous in the (001) plane.[65,66] However, we have found that the complete

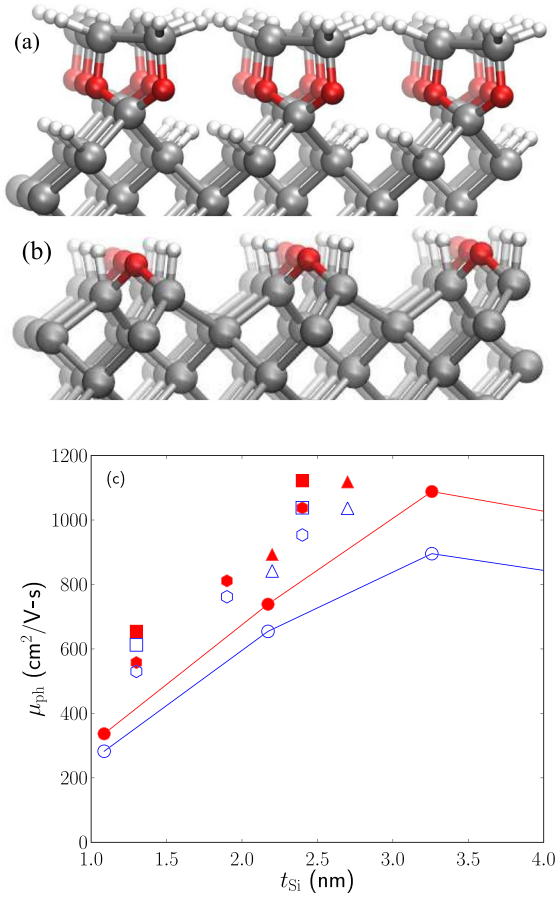

FIG. 7. (a) First model of oxidized surface (Model 1). The surface dangling bonds are saturated by O-Si-H_2 radicals. The Si atoms are represented by large-diameter gray spheres, O atoms by medium-diameter red spheres, and H atoms by small-diameter white spheres. (b) Same for the second model (Model 2) characterized by oxygen atoms inserted in Si dimers. (c) Phonon-limited electron mobility in (001) Si films. Circles and squares: H-passivated surfaces. Triangles: oxidized surfaces, Model 1. Hexagons: oxidized surfaces, Model 2. The results are plotted for $n = 1 \times 10^{12}$ cm^{-2} (red color, filled markers) and $n = 5 \times 10^{12}$ cm^{-2} (blue color, empty markers). All calculations have been performed using the Tersoff potential except those represented by circles for H-passivated surfaces performed using the VFF model of Vanderbilt *et al.*

relaxation of these models using the Tersoff potential leads to very important strains (>5%) in the Si film, which are not realistic. Therefore, these models cannot be used to compute carrier mobilities that are very sensitive to strains.[40,67] The latter are likely reduced when the Si film is embedded in an amorphous oxide, but this situation cannot be studied using the present methods limited to periodic systems with small unit cells.

The band structure and mobility are calculated once again as described in Sec. II B. The TB parameterization for Si-O bonds is given in Appendix D.

B. Tersoff model for phonons

Before discussing the influence of the oxidation, it is interesting to investigate the effects of the replacement of the VFF model of Vanderbilt *et al.* by the Tersoff potential on the results for hydrogen-passivated films. Figure 7(c) shows that the electron mobility at 300 K takes higher values with the Tersoff than with the Vanderbilt model, the difference being as large as 33% in a 2.4 nm thick film at carrier density $n \sim 10^{12}$ cm^{-2}. We have found that this discrepancy mainly results from the bad description of the transverse acoustic (TA) modes with energies above ~10 meV by the Tersoff potential, as shown in Appendix C. As a matter of fact, the mobilities predicted by the two potentials agree within a few percent when only phonons below 10 meV are considered, or at $T = 77$ K, i.e., when higher energy phonons do not contribute to the scattering of electrons. This demonstrates the importance of using accurate descriptions of the phonon band structure in order to get reliable results.

C. Influence of the surface passivation on the electron mobility

It is nevertheless relevant to compare the mobilities obtained with the Tersoff potential for different surface passivations. The comparisons are restricted to electrons, and to thin films, due to computational limitations. Figure 7(c) shows that the mobilities in oxidized films are smaller than in hydrogen-passivated films, though the difference remains small. Quite similar results are obtained for structural Models 1 and 2. The effect of the oxidation should be even smaller for thicker films, when the carriers are less sensitive to the surface. We conclude that the phonon-limited electron mobility is not considerably degraded by the presence of an oxide, at least in the absence of interface roughness and strain, and in the absence of "remote" phonon scattering by polar optical phonons in the gate stack.[20,32]

V. TRANSITION FROM Si FILMS TO Si NANOWIRES

The present methodology can also be applied to bulk[37] and nanowires.[38–40] It therefore provides an unique, consistent description of the effects of dimensionality on the transport properties of silicon nanostructures. In this section, we investigate, in particular, the transition from 2D films to 1D nanowires.

Figure 8 shows the evolution of the electron and hole mobilities when going from [110] nanowires of rectangular section to (001) films (at low carrier density $n \to 0$). The $1 \times n$ nanowires with characteristic size d have $(1\bar{1}0)$ facets with height $H = d$ and (001) facets with width $W = nd$. The huge differences between the mobility in nanowires and films highlight the effects of quantum confinement on the electronic band structure, on the electron-phonon interactions, and therefore on the transport properties of these nanostructures.[38–40,57,58] Interestingly, the behaviors of the electron (Fig. 8(a)) and hole (Fig. 8(b)) mobilities are very different.

The lowest conduction bands in both (001) films and [110] nanowires pertain to twofold degenerate valleys with a light effective mass ($m^* \leq 0.19 m_0$).[39] These can be identified as the projection of the bulk Si Δ_z valleys at the Γ point of the Brillouin zone. In both cases, the conduction band minima at higher energy and $k \neq 0$ are derived from the Δ_x and Δ_y valleys with larger effective mass.[39,68] However, the splitting $\Delta E = E(\Delta_{x,y}) - E(\Delta_z)$ between the heavy and light valleys is smaller in [110] nanowires than in (001) films

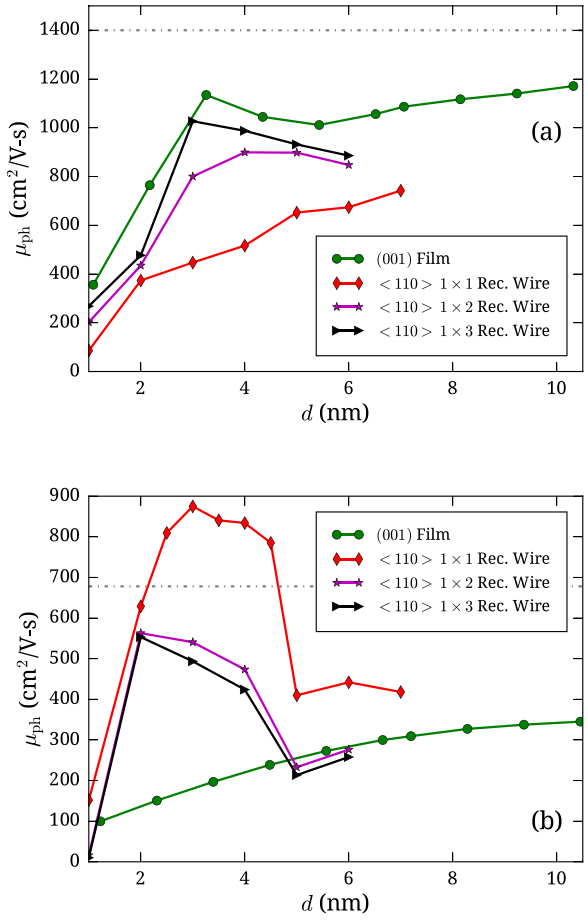

FIG. 8. (a) Phonon-limited electron mobility in (001) Si films with thickness d (green circles), square [110] Si nanowires with side d (red lozenges), and rectangular [110] Si ribbons with sides $d \times 2d$ (magenta stars) and $d \times 3d$ (black triangles). The horizontal line indicates the calculated bulk Si mobility. (b) Same for holes.

with the same thickness d because lateral confinement rises the light Δ_z faster than the heavier $\Delta_{x,y}$ valleys and hence reduces ΔE with respect to films. Therefore, the population of electrons in the heavy mass valleys is larger in nanowires than in films. Lateral confinement also enhances the interactions between electrons and acoustic phonons.[7,13,56] The mobility of electrons is hence smaller in square [110] nanowires than in (001) films. It rapidly tends, however, to the mobility in (001) films when increasing the width of the nanowires.

In contrast with electrons, the mobility of holes is considerably larger in square [110] nanowires than in (001) films, up to a factor 4 for $d \approx 3$–4 nm (Fig. 8(b)). However, it draws rapidly near the mobility in (001) films when increasing W. This behavior results from the effects of lateral confinement on the valence bands. Indeed, lateral confinement tends to promote bands with a light hole character along the nanowire axis.[39,68] Therefore, the effective mass of the holes decreases when going from (001) films to [110] nanowires, and the mobility increases despite the enhancement of the coupling to acoustic phonons. The transition from wires to films is, as expected, faster in weakly confined structures with large characteristic size d.

VI. COMPARISON WITH KP-NEGF AND DISCUSSION ON THE ACOUSTIC DEFORMATION POTENTIALS

In this section, we compare the mobilities computed in the above semi-classical Kubo-Greenwood plus tight-binding framework (TB-KG), with the mobilities computed in the NEGF framework using $\mathbf{k} \cdot \mathbf{p}$ models for the band structure and deformation potentials for the electron-phonon interactions (hereafter denoted KP-NEGF). We use these comparisons to discuss issues about the magnitude of the acoustic deformation potentials. The section begins with a short review of the literature on this topic.

A. Experimental evidence of enhanced acoustic deformation potentials

While for $t_{Si} > 20$ nm the electron mobility shows the same behavior in SOI as in bulk MOSFETS,[7,69,70] it is significantly degraded in thinner films, especially for $t_{Si} < 10$ nm,[7,11,23,71,72] and the degradation is stronger than in bulk MOSFETs for a given effective field.[54,55,73] One of the reasons put forward to explain this degradation is the enhancement of electron-phonon interactions.

In device simulations,[30,49] electron-phonon scattering is usually modeled with the deformation potential theory. In its simplest form, the carrier-phonon interaction is characterized by a single, effective acoustic deformation potential Ξ^e_{ac} (Ξ^h_{ac} for holes). Due to the anisotropy of the conduction band valleys of bulk Si, Ξ^e_{ac} is defined as an average of the deformation potential over initial states of constant energy and over all possible angles of scattering (see Refs. 74 and 30, and Appendix B). Lumping all interactions into the dominant coupling to longitudinal acoustic (LA) phonons, a value for Ξ^e_{ac} around 9–10 eV yields $\mu \simeq 1400$ cm^2/V s for electrons in bulk Si, in good agreement with experiments.[49]

The deformation potential theory predicts an enhancement of electron-phonon scattering in inversion layers and thin films, which results from the increase of the overlap between the squared wave functions of the confined initial and final states.[7,13] This enhancement is not, however, strong enough to explain the experimental data. As a consequence, Ξ^e_{ac} must be significantly increased in order to reproduce the experimental mobilities in both bulk Si MOSFETs[29,55] and SOI devices.[7,13] As a matter of fact, $\Xi^e_{ac} \approx 12$ eV is often used in simulations on bulk MOSFETs.[55,75] An even higher value $\Xi^e_{ac} = 14.6$ eV is widely used in simulations on FDSOI and Si nanowire FETs,[6,13,48,76,77] which corresponds to an increase of roughly 50% with respect to the bulk. To solve this issue, other authors have introduced a spatially dependent Ξ^e_{ac}, which sharply increases close to the interfaces with the oxide.[11,25,78]

The reality of this enhancement could be questioned since the mobility in bulk MOSFETs and FDSOI devices results from a complex interplay between carrier-phonon interactions, interface roughness,[17,79,80] and Coulomb scattering.[20,32,35] However, experiments show that the low-temperature (25 K) mobility in FDSOI devices is the same for $t_{Si} = 60$ nm and $t_{Si} = 7.2$ nm, whereas at room temperature the mobility is much smaller for $t_{Si} = 7.2$ nm than for $t_{Si} = 60$ nm.[7] This demonstrates that the degradation of the mobility in thin films is due to a large extent to a

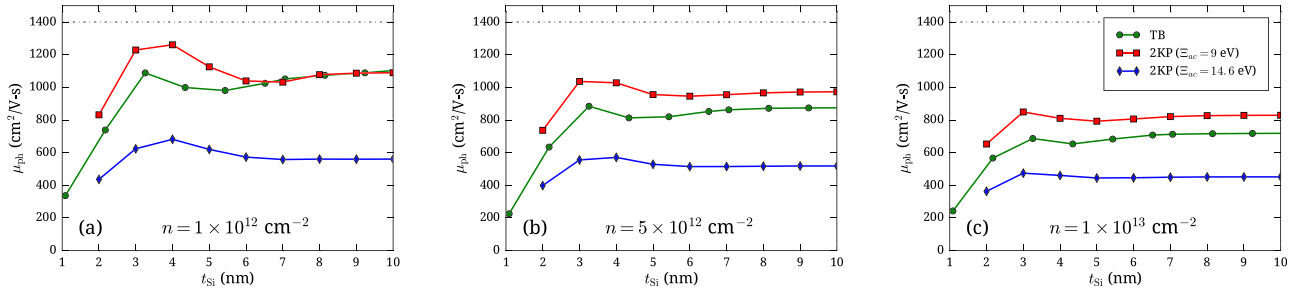

FIG. 9. Electron mobility in Si films. Comparison between TB-KG (green circles) and KP-NEGF calculations with $\Xi^e_{ac} = 9$ eV (red squares) and $\Xi^e_{ac} = 14.6$ eV (blue lozenges). (a) $n = 10^{12}$ cm^{-2}; (b) $n = 5 \times 10^{12}$ cm^{-2}; (c) $n = 10^{13}$ cm^{-2}. The horizontal line at 1400 cm^2/V s is the experimental mobility in bulk Si.

temperature dependent mechanism, which is readily identified as electron-phonon scattering.

The enhancement of Ξ^e_{ac} is also confirmed by a recent work combining NEGF calculations and experiments, which shows that Ξ^e_{ac} must be close to 15 eV in thin FDSOI devices.[24] Similarly, for holes, Ξ^h_{ac} must be increased from 10.2 eV, the bulk value, to 15.5 eV. This conclusion was reached by playing with the top- and back-gate biases independently in such a way that the carrier density at the Si-SiO_2 interfaces is minimized. In that limit, surface roughness scattering and remote Coulomb scattering become considerably weaker than phonon scattering (up to a factor 6 for electrons, 10 for holes), so that the phonon-limited mobility can be safely de-embedded by a comparison between theory and experiments.[24]

Therefore, the enhancement of the acoustic deformation potential in inversion layers can be considered as an established fact, although its origin remains largely ununderstood. In particular, it is not clear whether it follows from the failure of the deformation potential theory and of the approximations behind (isotropic average deformation potentials), or if it can be physically related to the effects of confinement on the electrons and phonons, or to the presence of an interface with an oxide. In the following, we try to shed new light on this important problem by comparing the mobilities calculated with the atomistic methodology and with the KP-NEGF approach based on deformation potentials.

B. Electron mobility: Comparison with KP-NEGF calculations

Three important facts must be pointed out about the relevance of the comparison between the different calculations. First, the average deformation potential $\Xi^e_{ac} = 8.6$ eV extracted from the TB calculations (Appendix B) is very close to the value (9–10 eV) commonly used in bulk Si. Second, it was shown in Refs. 23 and 81 that quantum NEGF and semi-classical KG calculations predict similar phonon-limited electron mobilities in Si films and wires if the same models are used for the band structures and for the electron-phonon interactions. Third, KP-NEGF calculations using $\Xi^e_{ac} = 14.6$ eV reproduce very well the experimental mobilities on FDSOI devices in a wide range of carrier densities, back gate biases, and temperatures.[24]

The TB-KG and KP-NEGF mobilities are compared in Fig. 9. For $n \sim 10^{12}$ cm^{-2}, KP-NEGF with the bulk $\Xi^e_{ac} = 9$ eV and TB-KG predict similar results, especially for large t_{Si}. This supports the widely used approximation of an average deformation potential independent of energy and scattering angle (Appendix B).[74,82] For larger carrier densities and for very thin films (Figs. 9(b) and 9(c)), TB-KG predict smaller mobilities than KP-NEGF with $\Xi^e_{ac} = 9$ eV. In this regime where the electrons are strongly confined near the top interface of the film, it is not surprising that atomistic (TB) and continuous ($\mathbf{k} \cdot \mathbf{p}$) descriptions deviate. The isotropic deformation potential approximation might also break down in that limit. However, the TB-KG mobilities remain much larger than the KP-NEGF mobilities with $\Xi^e_{ac} = 14.6$ eV that reproduce the experimental data on FDSOI devices. Therefore, the atomistic TB-KG calculations capture only part of the mobility degradation measured in thin film devices.

C. Hole mobility: Comparison with KP-NEGF calculations

The comparison (Fig. 10) between TB-KG and KP-NEGF is less straightforward for holes than for electrons because the

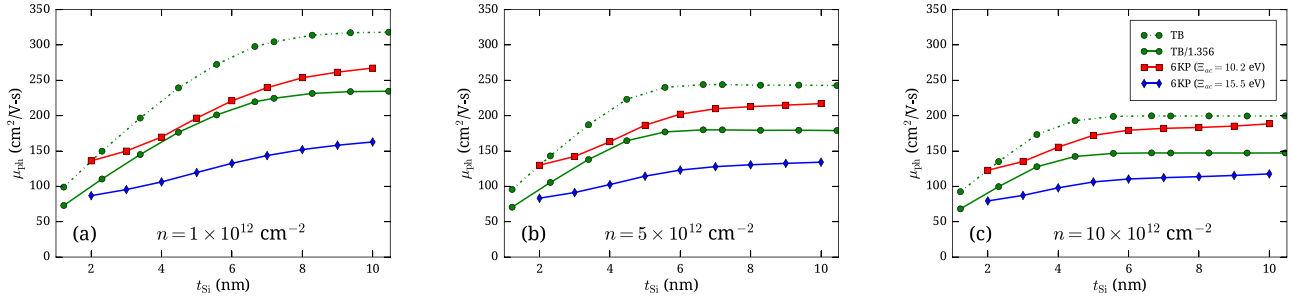

FIG. 10. Hole mobility in Si films. Comparison between TB-KG calculations (green circles) and KP-NEGF calculations with $\Xi^h_{ac} = 10.2$ eV (red squares) and $\Xi^h_{ac} = 15.5$ eV (blue lozenges). (a) $n = 10^{12}$ cm^{-2}; (b) $n = 5 \times 10^{12}$ cm^{-2}; (c) $n = 10^{13}$ cm^{-2}. The green dotted lines are the original TB values, while the green solid lines are rescaled by a factor 1/1.356 in order to account for the difference between the experimental and TB-KG bulk mobility.

TB-KG bulk hole mobility ($678\,cm^2/V\,s$) overestimates the experimental result by 35.6%.[39] For the sake of comparison, we have therefore rescaled the TB-KG mobilities by a factor 1/1.356 in Fig. 10. The original mobilities are also shown as dotted lines for reference.

The comparison between the TB-KG and KP-NEGF calculations leads to the same conclusions for holes as for electrons (Sec. VI B). For $n \sim 10^{12}\,cm^{-2}$, the rescaled TB-KG mobilities are close to the KP-NEGF mobilities calculated with the bulk $\Xi^h_{ac} = 10.2\,eV$. However, when n is increased, the rescaled TB-KG mobilities decrease faster than the KP-NEGF mobilities. Interestingly, for $n = 10^{13}\,cm^{-2}$, the TB-KG mobilities are not far from the KP-NEGF data calculated with $\Xi^h_{ac} = 15.5\,eV$ (but they are still larger). This shows, again, that TB-KG is able to capture part—but only part—of the enhancement of the interaction with acoustic phonons in thin films.

D. Discussion about the acoustic deformation potentials

We can summarize the conclusions from the above comparisons as follows: First, there is, at low carrier density, a close agreement between TB-KG and KP-NEGF calculations with bulk, isotropic deformation potentials. This supports the validity of the simplest deformation potential models for $n \lesssim 3 \times 10^{12}\,cm^{-2}$. Second, the TB-KG mobility decreases faster than the KP-NEGF mobility with decreasing film thickness and with increasing carrier density. The effects of confinement are, indeed, a bit stronger in TB. The TB-KG mobilities remain nonetheless significantly larger than the KP-NEGF mobilities calculated with the enhanced deformation potentials that match the experimental data—especially at low carrier density. Therefore, a significant part of the expected enhancement of the electron-phonon interactions does not naturally come out from the atomistic TB calculations. The confinement of the carriers and phonons, which is in principle well described by the TB-KG calculations, cannot explain it alone. Moreover, the introduction of oxidized surfaces in the atomistic models does not result in a significant decrease of the electron mobility (see Sec. IV).

The validity of Boltzmann's equation can hardly be questioned, at least for electrons, since the KG and NEGF mobilities are very close if the same band structures and electron-phonon interactions are used as input for both.[23,81] Therefore, we believe that the possible deficiencies of the KG approach cannot explain why the electron mobilities are overestimated by TB-KG in thin films.

The reasons why TB-KG overestimates the hole mobility in bulk Si are, admittedly, more intriguing, as the TB model reproduces all valence band deformation potentials. The first order perturbation theory (Fermi Golden Rule) used in TB-KG might be less accurate in the nearly degenerate heavy- and light-hole bands of silicon.[39] In this respect, the diagonal deformation potential model used in NEGF calculations is very simplistic as it decouples the heavy- and light-hole bands. The comparison between KG and NEGF calculations based on this deformation potential model would not, therefore, be conclusive as to the validity of Boltzmann transport equation for holes.

We now discuss other possible reasons why TB-KG overestimates electron and hole mobilities in thin films. Of course, we cannot exclude that TB, a semi-empirical method, underestimates the scattering rates and the effects of confinement on the electron-phonon coupling. It must be noticed, however, that the TB scattering rates tend to be larger than the *ab initio* scattering rates in bulk Si.[83] Therefore, density functional theory would not likely give a different picture –at least when the electron-phonon matrix elements are computed (as is usually the case) in the insulating ground state. It would, however, be interesting to understand better the effects of band filling on these matrix elements.

As discussed in Sec. IV, strains at the Si/SiO_2 interface—as well as subtle interactions between different scattering mechanisms—might change the apparent deformation potentials. Surface roughness and structural disorder in the oxides could, in particular, scatter the phonons and alter the electron-phonon coupling. It has for example, been shown in graphene[84] that a slight admixture of optical phonon components into the acoustic branches can have a significant impact on the net acoustic deformation potential. Such interactions are, however, beyond the reach of our calculations, which are restricted to small unit cells at present.

VII. CONCLUSION

We have investigated the phonon-limited carrier mobility in (001) Si films using atomistic methods (tight-binding for electrons and valence force field for phonons). The scattering rates have been computed from the electron and phonon wave functions with the Fermi golden rule and the mobilities from an exact solution of Boltzmann transport equation. All possible carrier-phonon scattering processes have been included in the calculations.

The electron and hole mobilities are always found smaller in Si films than in bulk Si. They basically decrease when the film is thinned down and when the carrier density (or electric field) is increased, as the structural and electric confinement enhance the carrier-phonon interactions. The comparison between the mobilities in Si films and in Si nanowires gives further insights into the effects of quantum confinement and dimensionality on the transport properties of silicon. In order to understand the impact of surface passivation, we have also compared Si films with hydrogenated or oxidized surfaces. The electron mobilities are actually similar in both cases, at least in the absence of disorder and strains.

Non-Equilibrium Green's Functions calculations based on $\mathbf{k} \cdot \mathbf{p}$ band structures and bulk-Si deformation potentials for the carrier-phonon interactions yield mobilities in good agreement with TB calculations at low carrier density. Therefore, atomistic TB calculations cannot explain why the acoustic deformation potentials need to be systematically enhanced by around 50% in the simulation of FDSOI devices, and more generally in confined 2D Si systems, in order

to match the experimental mobilities. We suggest that this enhancement could result from a subtle interplay between electron-phonon interactions and other scattering processes, such as surface roughness scattering. Further studies are thus needed to solve this important issue.

ACKNOWLEDGMENTS

We thank François Triozon and Ivan Duchemin for helpful discussions. This work was supported by the French National Research Agency (ANR) project "NOODLES" ANR-13-NANO-0009-02. Part of the calculations were run on the TGCC/Curie machine using allocations from GENCI and PRACE. The authors acknowledge fruitful exchanges with Alfredo Pasquarello.

APPENDIX A: NUMERICAL DETAILS

The electron and hole states are calculated on a non-homogeneous triangular mesh in the Brillouin zone. The mesh is much denser in the areas where the electronic bands are close to the Fermi level. The phonons are calculated on a regular square mesh.

The scattering processes are searched using the algorithm (1). The wave-vector $\mathbf{k}$ of the initial electron state runs over the nodes of the triangular mesh and the energy E of this state runs over all bands. For each initial state, we look for possible final states in all triangles. Let $\mathbf{k}_j$ ($j = 1, 2, 3$) be the vertices of a triangle, and E_j the energies of a band at these vertices. The phonon energies $\hbar\omega_j$ of each phonon band are first bi-linearly interpolated from the square mesh to the wave-vectors $\mathbf{q}_j = \mathbf{k}_j - \mathbf{k}$. To test for phonon absorption, we then compute the energies $\delta E_j = E_j - (E + \hbar\omega_j)$ on the three vertices. There are possible final states in the triangle if the three δE_j do not have the same sign. A similar algorithm is used for holes and for phonon emission processes.

ALGORITHM I. Searching for scattering events (phonon absorption).

```
for each node in the triangular mesh (initial state) do
  for each electron band (initial state) do
    for each triangle (final state) do
      q_j = k_j − k
      for each electron band (final state) do
        for each phonon band do
          interpolate ħω_j
          compute δE_j = E_j − (E + ħω_j)
          if min(δE_j) <= 0 and max(δE_j) >= 0 then
            compute scattering rate
          end if
        end for
      end for
    end for
  end for
end for
```

On each such triangle, the final states are assumed to be on the line $\delta E = 0$ obtained from the interpolation of the δE_j's within the triangle. The scattering rates along this line are then written as linear combinations of the scattering rates on the vertices of the triangle using barycentric coordinates. The scattering matrix elements for a given phonon wave-vector $\mathbf{q}_j$ are computed using the phonon wave functions at the closest $\mathbf{q}$ vector on the square mesh.

Typically, for $t_{\mathrm{Si}} = 10\,\mathrm{nm}$, we use a mesh of 14 332 triangles in the Brillouin zone, 5000 $\mathbf{q}$ vectors, 32 electron bands, and 240 phonon bands.

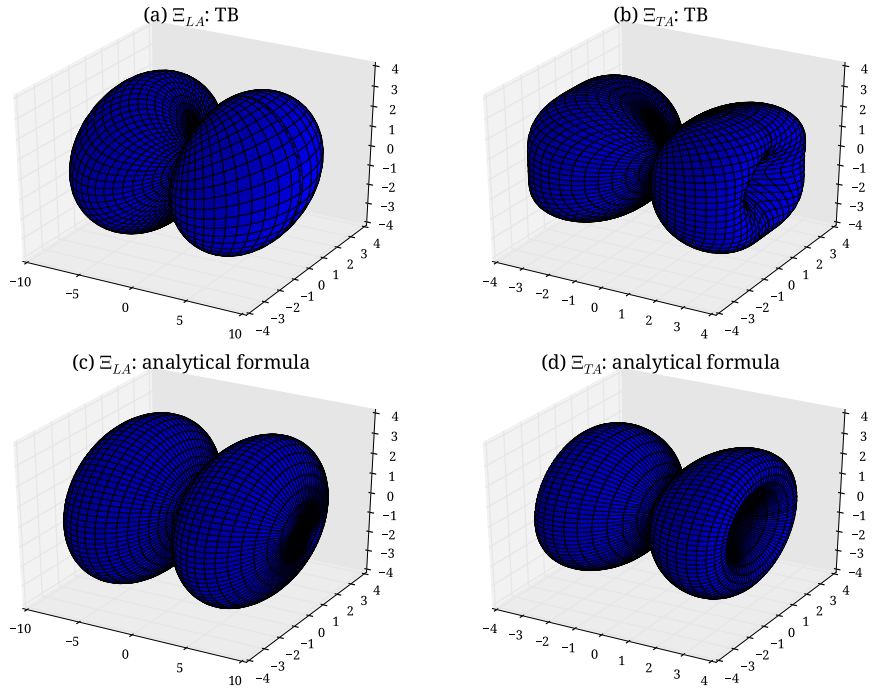

FIG. 11. Angular-dependent deformation potentials for the coupling to LA [(a) and (c)] and TA [(b) and (d)] phonons derived from TB calculations [(a) and (b)], or calculated using Eq. (B2) with $\Xi_d = 0.91\,\mathrm{eV}$ and $\Xi_u = 8.70\,\mathrm{eV}$ (c), (d).

APPENDIX B: BULK SI ELECTRON DEFORMATION POTENTIALS CALCULATED IN TB

In the first part of this section, we show that magnitude and angular dependence of the TB intra-valley scattering rates are consistent with the deformation potential theory for electrons in bulk Si. In the second part, we extract a value for the average deformation potential Ξ_{ac}^{e} from the TB calculations.

1. Anisotropic scattering rates and deformation potentials

We consider scattering events taking place between the electronic states of a given valley of silicon, at energies close to the conduction band edge, where non-parabolic corrections are negligible. The scattering rates may be written as $R = (2\pi/\hbar)|M(\theta,\phi)|^2\left(N_b + \frac{1}{2} \pm \frac{1}{2}\right)\delta(\Delta E \pm \hbar\omega_{ph})$, where ΔE is the difference between the energies of the final and initial states, and N_b is the average number of phonons with energy $\hbar\omega_{ph}$ at room temperature (Bose-Einstein factor). Due to the anisotropy of the valley,[30,74] the electron-phonon interaction matrix element $M(\theta,\phi)$ must depend on the angle θ between the wave vector $\mathbf{q}$ of the emitted/absorbed phonon and the longitudinal axis of the valley, but should in principle be independent of the polar angle ϕ. From $M(\theta,\phi)$, we can define an effective angular-dependent deformation potential[49]

$$\Xi(\theta,\phi) = \frac{|M(\theta,\phi)|^2}{|\mathbf{q}|}\sqrt{\frac{2NM_{Si}\omega_{ph}}{\hbar}}, \tag{B1}$$

where M_{Si} is the mass of a Si atom and N is the number of atoms per unit cell.

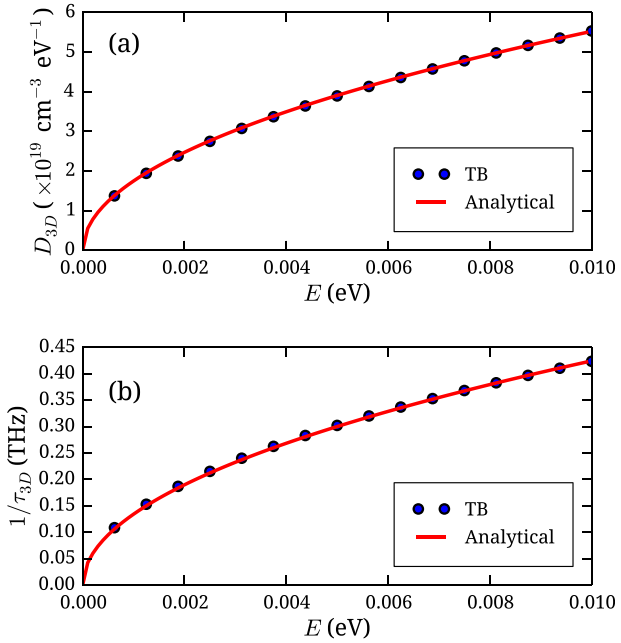

FIG. 12. (a) Density of states in the lowest conduction band of bulk Si (blue dots). The solid line is proportional to $\sqrt{E}$. (b) Average scattering rate calculated for electrons on a constant energy surface of the conduction band of bulk Si, versus energy (blue dots). Solid line: analytical fit using Eq. (B3).

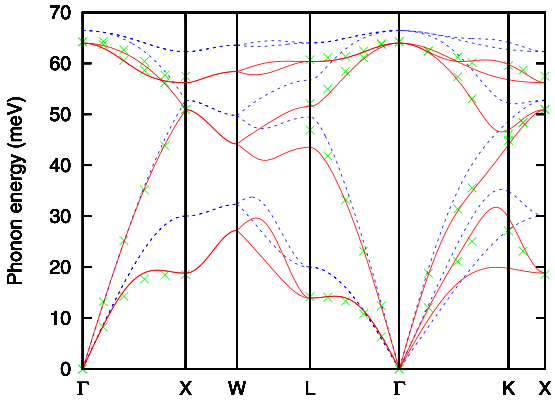

FIG. 13. Phonon band structure of Si calculated using Tersoff[59] (blue dashed lines) and Vanderbilt *et al.*[45] (red solid lines) potentials compared to the experimental data of Ref. 85 (green crosses).

$\Xi(\theta,\phi)$ is plotted in Figs. 11(a) and 11(b) for the longitudinal (LA) and transverse (TA) acoustic phonons. For TA phonons, the deformation potential is an average over the two TA branches, i.e., $\Xi_{TA} = (\Xi_{TA1}^2 + \Xi_{TA2}^2)^{1/2}$. As shown in Figs. 11(c) and 11(d), Ξ_{LA} and Ξ_{TA} match the deformation potential theory[74]

$$\begin{aligned}\Xi_{LA} &= \Xi_d + \Xi_u \cos^2\theta \\ \Xi_{TA} &= \Xi_u \sin\theta\cos\theta,\end{aligned} \tag{B2}$$

where[41] $\Xi_d = 0.91$ eV and $\Xi_u = 8.70$ eV describe the response of the conduction band edge to dilation and shear deformations, respectively. The TB deformation potentials show a small dependence on ϕ because the valley only has a fourfold symmetry axis at the atomistic level. We conclude that our TB description is consistent with the deformation potential theory for intra-valley scattering at low energy.

2. Average scattering rates and deformation potential

As discussed in Sec. VI A, most simulations of Si devices do not make use of the above angular-dependent deformation potentials but assume an isotropic deformation potential, which is often adjusted on experiments. In the

TABLE I. TB parameters (notations of Slater and Koster[42]) for SiO_2 in an orthogonal sp^3 model. The Si-O and O-O hopping matrix elements are assumed to depend on the Si-O (d_{SiO}) and O-O (d_{OO}) distances as $(d_{SiO}^0/d_{SiO})^2$ and $(d_{OO}^0/d_{OO})^2$, respectively, with $d_{SiO}^0 = 1.60$ Å and $d_{OO}^0 = 2.61$ Å.

Parameters for SiO_2 (eV)			
E_s(Si)	3.10	E_s(O)	−21.40
E_p(Si)	5.60	E_p(O)	−6.20
$V_{ss\sigma}$(SiO)	−2.80	$V_{ss\sigma}$(OO)	−0.50
$V_{sp\sigma}$(SiO)	3.70	$V_{sp\sigma}$(OO)	0.00
$V_{sp\sigma}$(OSi)	5.70		
$V_{pp\sigma}$(SiO)	5.30	$V_{pp\sigma}$(OO)	0.86
$V_{pp\pi}$(SiO)	−1.40	$V_{pp\pi}$(OO)	−0.33
Parameters for Si-H and O-H (eV)			
E_H	0.00		
$V_{ss\sigma}$	−35.70	$V_{sp\sigma}$	61.83

following, we derive the isotropic deformation potential Ξ_{ac}^{e} of bulk Si from the TB calculations. For that purpose, we first compute the scattering rates from the initial states on a surface of constant energy in a given conduction band valley. We then average the scattering rates over both initial and final states in that valley, so that the result only depends on the initial carrier energy.

The average scattering rate calculated in that way is plotted in Fig. 12(b). Its variations with the electron energy E are fully consistent with the following expression for the electron-phonon scattering rate $1/\tau_{3D}(E)$:[49]

$$\frac{1}{\tau_{3D}(E)} = \frac{k_B T \Xi_{ac}^{e\,2} \pi D_{3D}(E)}{\hbar v_s^2 \rho}, \tag{B3}$$

where $v_s = 9040\,\text{m/s}$ is the velocity of LA phonons, $\rho = 2.329\,\text{g/cm}^3$ is the mass density of silicon, and $D_{3D}(E) \propto \sqrt{E}$ is the density of states. Using the TB $D_{3D}(E)$ (Fig. 12(a)), Eq. (B3) reproduces the scattering rates of Fig. 12(b) with $\Xi_{ac}^{e} = 8.6\,\text{eV}$, which is close to the value of ~9 eV adjusted on experimental data for bulk Si.

APPENDIX C: PHONON BAND STRUCTURES FOR BULK Si

Figure 13 shows that the phonon dispersion curves of the VFF model of Vanderbilt *et al.*[45] are in excellent agreement with inelastic neutron scattering experiments.[85] In comparison, the longitudinal acoustic (LA) and transverse acoustic (TA) sound velocities are correctly given by the Tersoff potential,[59] but the optical phonon branches are too high and, above all, the energy of the TA branch at the L and X points of the Brillouin zone is strongly overestimated, a common problem with descriptions based on atomistic interatomic potentials.[86]

APPENDIX D: TIGHT-BINDING MODEL FOR SiO_2

The TB model used in the present work to describe Si-O bonds has been developed for the more general purpose of modeling the band structure of silicon oxides (unpublished). The idea was to build a simple model that can be applied to different forms of crystalline or amorphous SiO_2 with a reasonable accuracy. Silicon and oxygen atoms are represented by one s and three p orbitals, spin-orbit coupling is neglected, and the hopping matrix elements are restricted to nearest-neighbor Si-O interactions and to interactions between oxygen atoms sharing a common Si neighbor. The TB parameters are given in Table I. For convenience, the reference of energy for the on-site terms is defined so that the top of the valence band of the ideal β-cristobalite SiO_2 crystal (space group $Fd3m$) is at $-4.4\,\text{eV}$, i.e., close to the valence band offset at Si/SiO_2 interfaces. In spite of its simplicity, this TB model predicts band structures (Fig. 14) in relatively good agreement with *ab initio* calculations for ideal β-cristobalite[87] and α-quartz structures.[88] Detailed studies of crystalline and amorphous SiO_2 compounds using this TB model will be published in a specific paper.

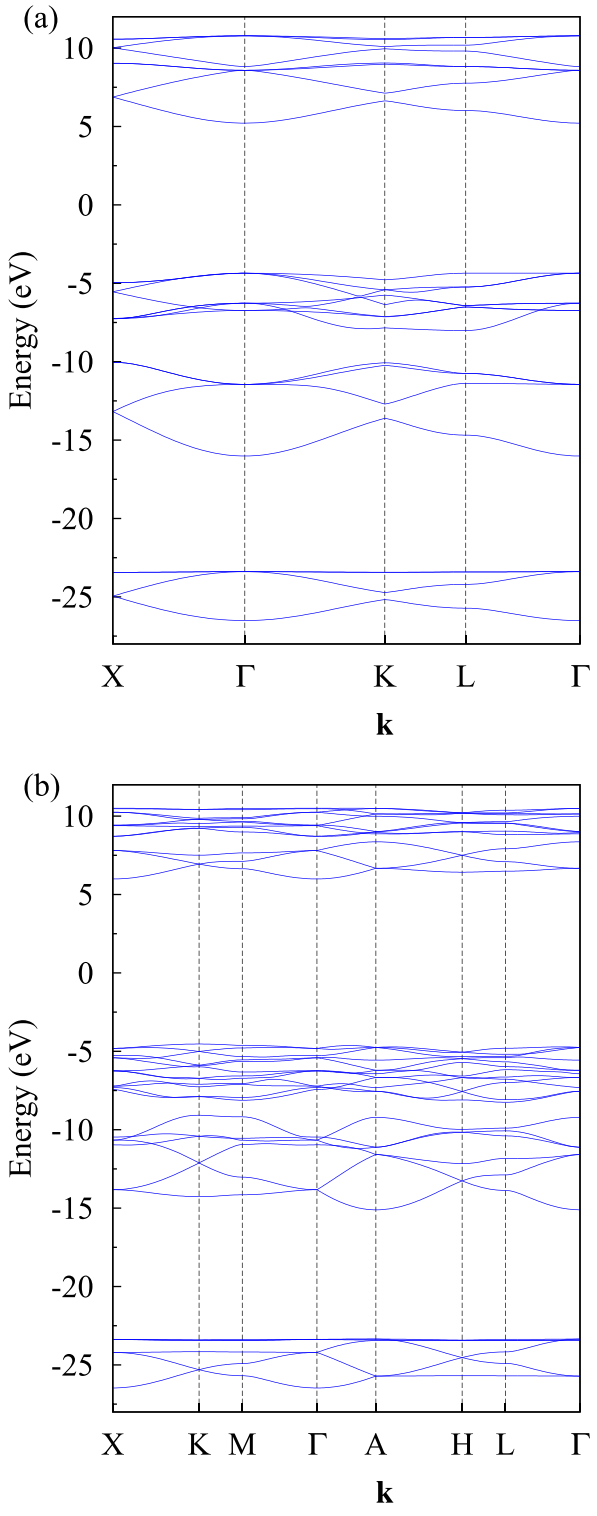

FIG. 14. Band structure of SiO_2 crystals with the β-cristobalite (a) and α-quartz (b) lattices.

Table I also provides the parameters for the Si-H and O-H bonds, which are present in the model structures of oxidized surfaces studied in Sec. IV.

[1]See http://www.itrs.net/ for The International Technology Roadmap for Semiconductors (ITRS).

[2]Y. Taur, D. Buchanan, W. Chen, D. Frank, K. Ismail, S.-H. Lo, G. Sai-Halasz, R. Viswanathan, H.-J. Wann, S. Wind, and H.-S. Wong, IEEE Proc. **85**, 486 (1997).

[3]F. Balestra, S. Cristoloveanu, M. Benachir, J. Brini, and T. Elewa, IEEE Electron Device Lett. **8**, 410 (1987).
[4]G. K. Celler and S. Cristoloveanu, J. Appl. Phys. **93**, 4955 (2003).
[5]J.-P. Colinge, Solid-State Electron. **48**, 897 (2004).
[6]D. Esseni and E. Sangiorgi, Solid-State Electron. **48**, 927 (2004).
[7]K. Uchida, J. Koga, and S. Takagi, J. Appl. Phys. **102**, 074510 (2007).
[8]C. Fenouillet-Beranger, S. Denorme, B. Icard, F. Boeuf, J. Coignus, O. Faynot, L. Brevard, C. Buj, C. Soonekindt, J. Todeschini, J. Le-Denmat, N. Loubet, C. Gallon, P. Perreau, S. Manakli, B. Mmghetti, L. Pain, V. Arnal, A. Vandooren, D. Aime, L. Tosti, C. Savardi, F. Martin, T. Salvetat, S. Lhostis, C. Laviron, N. Auriac, T. Kormann, G. Chabanne, S. Gaillard, O. Belmont, E. Laffosse, D. Barge, A. Zauner, A. Tarnowka, K. Romanjec, H. Brut, A. Lagha, S. Bonnetier, F. Joly, N. Mayet, A. Cathignol, D. Galpin, D. Pop, R. Delsol, R. Pantel, F. Pionnier, G. Thomas, D. Bensahel, S. Deleombus, T. Skotnicki, and H. Mmgam, Tech. Dig. - IEEE Int. Electron Devices Meet. **2007**, 267–270.
[9]C. Fenouillet-Beranger, S. Denorme, P. Perreau, C. Buj, O. Faynot, F. Andrieu, L. Tosti, S. Barnola, T. Salvetat, X. Garros, M. Cass, F. Allain, N. Loubet, L. Pham-Nguyen, E. Deloffre, M. Gros-Jean, R. Beneyton, C. Laviron, M. Marin, C. Leyris, S. Haendler, F. Leverd, P. Gouraud, P. Scheiblin, L. Clement, R. Pantel, S. Deleonibus, and T. Skotnicki, Solid-State Electron. **53**, 730 (2009).
[10]O. Faynot, F. Andrieu, O. Weber, C. Fenouillet-Beranger, P. Perreau, J. Mazurier, T. Benoist, O. Rozeau, T. Poiroux, M. Vinet, L. Grenouillet, J.-P. Noel, N. Posseme, S. Barnola, F. Martin, C. Lapeyre, M. Casse, X. Garros, M.-A. Jaud, O. Thomas, G. Cibrario, L. Tosti, L. Brevard, C. Tabone, P. Gaud, S. Barraud, T. Ernst, and S. Deleonibus, Tech. Dig. - IEEE Int. Electron Devices Meet. **2010**, 3.2.1–3.2.4.
[11]T. Ohashi, T. Takahashi, N. Beppu, S. Oda, and K. Uchida, Tech. Dig. - IEEE Int. Electron Devices Meet. **2011**, 16.4.1–16.4.4.
[12]N. Planes, O. Weber, V. Barral, S. Haendler, D. Noblet, D. Croain, M. Bocat, P. Sassoulas, X. Federspiel, A. Cros, A. Bajolet, E. Richard, B. Dumont, P. Perreau, D. Petit, D. Golanski, C. Fenouillet-Beranger, N. Guillot, M. Rafik, V. Huard, S. Puget, X. Montagner, M.-A. Jaud, O. Rozeau, O. Saxod, F. Wacquant, F. Monsieur, D. Barge, L. Pinzelli, M. Mellier, F. Boeuf, F. Arnaud, and M. Haond, in *2012 Symposium on VLSI Technology (VLSIT)* (2012) pp. 133–134.
[13]D. Esseni, A. Abramo, L. Selmi, and E. Sangiorgi, IEEE Trans. Electron Devices **50**, 2445 (2003).
[14]Z. Ren, R. Venugopal, S. Goasguen, S. Datta, and M. Lundstrom, IEEE Trans. Electron Devices **50**, 1914 (2003).
[15]L. Lucci, P. Palestri, D. Esseni, L. Bergagnini, and L. Selmi, IEEE Trans. Electron Devices **54**, 1156 (2007).
[16]S. Reggiani, E. Gnani, A. Gnudi, M. Rudan, and G. Baccarani, IEEE Trans. Electron Devices **54**, 2204 (2007).
[17]S. Jin, M. Fischetti, and T.-W. Tang, IEEE Trans. Electron Devices **54**, 2191 (2007a).
[18]A. Cresti, M. Pala, S. Poli, M. Mouis, and G. Ghibaudo, IEEE Trans. Electron Devices **58**, 2274 (2011).
[19]N. Cavassilas, F. Michelini, and M. Bescond, J. Appl. Phys. **109**, 073706 (2011).
[20]P. Toniutti, P. Palestri, D. Esseni, F. Driussi, M. D. Michielis, and L. Selmi, J. Appl. Phys. **112**, 034502 (2012).
[21]D. Rideau, Y.-M. Niquet, O. Nier, P. Palestri, D. Esseni, V.-H. Nguyen, F. Triozon, I. Duchemin, D. Garetto, L. Smith, L. Silvestri, F. Nallet, C. Tavernier, and H. Jaouen, in International Workshop on Computational Electronics (IWCE) (2013).
[22]N. Cavassilas, M. Bescond, H. Mera, and M. Lannoo, Appl. Phys. Lett. **102**, 013508 (2013).
[23]Y.-M. Niquet, V.-H. Nguyen, F. Triozon, I. Duchemin, O. Nier, and D. Rideau, J. Appl. Phys. **115**, 054512 (2014).
[24]V.-H. Nguyen, Y.-M. Niquet, F. Triozon, I. Duchemin, O. Nier, and D. Rideau, IEEE Trans. Electron Devices **61**, 3096 (2014).
[25]S. Koba, R. Ishida, Y. Kubota, H. Tsuchiya, Y. Kamakura, N. Mori, and M. Ogawa, Jpn. J. Appl. Phys., Part 1 **53**, 114301 (2014).
[26]F. Pereira, D. Rideau, O. Nier, C. Tavernier, F. Triozon, D. Garetto, G. Mugny, B. Sklenard, G. Hiblot, and M. Pala, in *2015 Joint International EUROSOI Workshop and International Conference on Ultimate Integration on Silicon (EUROSOI-ULIS)* (2015), pp. 49–52.
[27]F. Stern, Phys. Rev. Lett. **44**, 1469 (1980).
[28]T. Ando, A. B. Fowler, and F. Stern, Rev. Mod. Phys. **54**, 437 (1982).
[29]C. Jungemann, A. Emunds, and W. Engl, Solid-State Electron. **36**, 1529 (1993).
[30]M. V. Fischetti and S. E. Laux, Phys. Rev. B **48**, 2244 (1993).
[31]A. Svizhenko, M. P. Anantram, T. R. Govindan, B. Biegel, and R. Venugopal, J. Appl. Phys. **91**, 2343 (2002).
[32]M. V. Fischetti, D. A. Neumayer, and E. A. Cartier, J. Appl. Phys. **90**, 4587 (2001).
[33]M. V. Fischetti, Z. Ren, P. M. Solomon, M. Yang, and K. Rim, J. Appl. Phys. **94**, 1079 (2003).
[34]D. Esseni and A. Abramo, IEEE Trans. Electron Devices **50**, 1665 (2003).
[35]F. Gamiz, J. B. Roldan, J. E. Carceller, and P. Cartujo, Appl. Phys. Lett. **82**, 3251 (2003).
[36]A. Asenov, A. R. Brown, G. Roy, B. Cheng, C. Alexander, C. Riddet, U. Kovac, A. Martinez, N. Seoane, and S. Roy, J. Comput. Electron. **8**, 349 (2009).
[37]D. Rideau, W. Zhang, Y. M. Niquet, C. Delerue, C. Tavernier, and H. Jaouen, in *2011 International Conference on Simulation of Semiconductor Processes and Devices* (2011), pp. 47–50.
[38]W. Zhang, C. Delerue, Y.-M. Niquet, G. Allan, and E. Wang, Phys. Rev. B **82**, 115319 (2010).
[39]Y.-M. Niquet, C. Delerue, D. Rideau, and B. Videau, IEEE Trans. Electron Devices **59**, 1480 (2012).
[40]Y.-M. Niquet, C. Delerue, and C. Krzeminski, Nano Lett. **12**, 3545 (2012).
[41]Y. M. Niquet, D. Rideau, C. Tavernier, H. Jaouen, and X. Blase, Phys. Rev. B **79**, 245201 (2009).
[42]J. C. Slater and G. F. Koster, Phys. Rev. **94**, 1498 (1954).
[43]Y. M. Niquet, C. Delerue, G. Allan, and M. Lannoo, Phys. Rev. B **62**, 5109 (2000).
[44]R. Tubino, L. Piseri, and G. Zerbi, J. Chem. Phys. **56**, 1022 (1972).
[45]D. Vanderbilt, S. H. Taole, and S. Narasimhan, Phys. Rev. B **40**, 5657 (1989).
[46]In the NEGF calculations, the film axis $x = (001)$ and the transport axis $z = (100)$ are meshed with a 2 Å step. The system is invariant by translation along $y = (010)$, so that this axis is not meshed in real space. The reciprocal space is meshed with 129 k_y points from $k_y = -64\Delta k_y$ to $k_y = 64\Delta k_y$, with $\Delta k_y = 0.1$ nm–1. Only the $k_y \geq 0$ points are actually computed, the $k_y < 0$ data being deduced from time-reversal symmetry. All k_y points are coupled by the electron-phonon self-energy. At variance with Ref. 23, the NEGF equations are solved in real space (no coupled mode space approximation).
[47]V. Sverdlov, G. Karlowatz, S. Dhar, H. Kosina, and S. Selberherr, Solid-State Electron. **52**, 1563 (2008).
[48]S. Jin, M. V. Fischetti, and T.-W. Tang, J. Appl. Phys. **102**, 083715 (2007).
[49]C. Jacoboni and L. Reggiani, Rev. Mod. Phys. **55**, 645 (1983).
[50]Namely, the squared matrix element of the carrier-acoustic phonon interaction H_{ac} between states ψ_i and ψ_j reads:

$$|\langle\psi_i|H_{ac}|\psi_j\rangle|^2 = \frac{kT\Xi_{ac}^2}{\rho v_s^2}\int d^3\mathbf{r}\,|\psi_i^\dagger(\mathbf{r})\cdot\psi_j(\mathbf{r})|^2,$$

where Ξ_{ac} is the acoustic deformation potential, v_s is the longitudinal sound velocity, ρ is the mass density, and T is the temperature. $\psi_i^\dagger(\mathbf{r})\cdot\psi_j(\mathbf{r})$ is the local scalar product between the 2 components (2KP) or 6 components (6KP) of the $\mathbf{k}\cdot\mathbf{p}$ wavefunctions. For the hole-optical phonon interaction,

$$|\langle\psi_i|H_{op}|\psi_j\rangle|^2 = \frac{\hbar^2 DK_{op}^2}{2\rho E_{op}}\int d^3\mathbf{r}\,|\psi_i^\dagger(\mathbf{r})\cdot\psi_j(\mathbf{r})|^2\times\left(n_{op}+\frac{1}{2}\pm\frac{1}{2}\right),$$

where DK_{op} is the optical deformation potential, E_{op} is the optical phonon energy, and n_{op} is the number of optical phonons (Bose-Einstein factor). The + sign holds for optical phonon emission, and the –sign for optical phonon absorption.
[51]M. Luisier and G. Klimeck, Phys. Rev. B **80**, 155430 (2009).
[52](a), the limit $n \to 0$ corresponds to a non-selfconsistent calculation (no vertical electric field) with the Fermi-Dirac distribution replaced with Boltzmann distribution.
[53](b), a single point has been calculated for $t_{Si} = 14$ nm because calculations are computationally extremely demanding.
[54]J. A. Cooper and D. F. Nelson, J. Appl. Phys. **54**, 1445 (1983).
[55]K. Masaki, C. Hamaguchi, K. Taniguchi, and M. Iwase, Jpn. J. Appl. Phys., Part 1 **28**, 1856 (1989).
[56]P. Price, Ann. Phys. **133**, 217 (1981).
[57]M. Luisier, Appl. Phys. Lett. **98**, 032111 (2011).
[58]N. Neophytou and H. Kosina, Phys. Rev. B **84**, 085313 (2011).
[59]J. Tersoff, Phys. Rev. B **38**, 9902 (1988).

[60]S. Munetoh, T. Motooka, K. Moriguchi, and A. Shintani, Comput. Mater. Sci. **39**, 334 (2007).
[61]F. de Brito Mota, J. F. Justo, and A. Fazzio, J. Appl. Phys. **86**, 1843 (1999).
[62]J. D. Gale, J. Chem. Soc., Faraday Trans. **93**, 629 (1997).
[63]P. Smith and A. Wander, Surf. Sci. **219**, 77 (1989).
[64]Y. Miyamoto and A. Oshiyama, Phys. Rev. B **41**, 12680 (1990).
[65]A. Pasquarello, M. S. Hybertsen, and R. Car, Phys. Rev. Lett. **74**, 1024 (1995).
[66]A. Pasquarello, M. S. Hybertsen, and R. Car, Appl. Phys. Lett. **68**, 625 (1996).
[67]M. O. Baykan, S. E. Thompson, and T. Nishida, J. Appl. Phys. **108**, 093716 (2010).
[68]Y. M. Niquet, A. Lherbier, N. H. Quang, M. V. Fernández-Serra, X. Blase, and C. Delerue, Phys. Rev. B **73**, 165319 (2006).
[69]J. Wang, N. Kistler, J. Woo, and C. Viswanathan, IEEE Electron Device Lett. **15**, 117 (1994).
[70]M. Sherony, L. Su, J. Chung, and D. Antoniadis, IEEE Trans. Electron Devices **41**, 276 (1994).
[71]J.-H. Choi, Y.-J. Park, and H.-S. Min, IEEE Electron Device Lett. **16**, 527–529 (1995).
[72]K. Uchida, J. Koga, R. Ohba, T. Numata, and S.-I. Takagi, Tech. Dig. - Int. Electron Devices Meet. **2001**, 29.4.1–29.4.4.
[73]A. Pirovano, A. Lacaita, G. Ghidini, and G. Tallarida, IEEE Electron Device Lett. **21**, 34 (2000).
[74]C. Herring and E. Vogt, Phys. Rev. **101**, 944 (1956).
[75]S. Takagi, J. L. Hoyt, J. J. Welser, and J. F. Gibbons, J. Appl. Phys. **80**, 1567 (1996).
[76]K. Rogdakis, S. Poli, E. Bano, K. Zekentes, and M. G. Pala, Nanotechnology **20**, 295202 (2009).
[77]F. Balestra, *Nanoscale CMOS: Innovative Materials, Modeling and Characterization*, ISTE (Wiley, 2013).
[78]T. Ohashi, S. Oda, and K. Uchida, Jpn. J. Appl. Phys., Part 1 **52**, 04CC12 (2013).
[79]S. M. Goodnick, D. K. Ferry, C. W. Wilmsen, Z. Liliental, D. Fathy, and O. L. Krivanek, Phys. Rev. B **32**, 8171 (1985).
[80]K. Uchida and S. Takagi, Appl. Phys. Lett. **82**, 2916 (2003).
[81]R. Rhyner and M. Luisier, J. Appl. Phys. **114**, 223708 (2013).
[82]M. V. Fischetti and S. E. Laux, J. Appl. Phys. **80**, 2234 (1996).
[83]W. Li, Phys. Rev. B **92**, 075405 (2015).
[84]T. Sohier, M. Calandra, C.-H. Park, N. Bonini, N. Marzari, and F. Mauri, Phys. Rev. B **90**, 125414 (2014).
[85]G. Dolling, in *Proceedings of Symposium on Inelastic Scattering Neutrons in Solids and Liquids* (Chalk River, IAEA, Vienna, 1963), Vol. 2.
[86]L. J. Porter, J. F. Justo, and S. Yip, J. Appl. Phys. **82**, 5378 (1997).
[87]L. E. Ramos, J. Furthmüller, and F. Bechstedt, Phys. Rev. B **69**, 085102 (2004).
[88]E. K. Chang, M. Rohlfing, and S. G. Louie, Phys. Rev. Lett. **85**, 2613 (2000).